Chem Catalysis

CellPress

Article

Dynamic electrocatalysis: Examining resonant catalytic rate enhancement under oscillating electrochemical potential

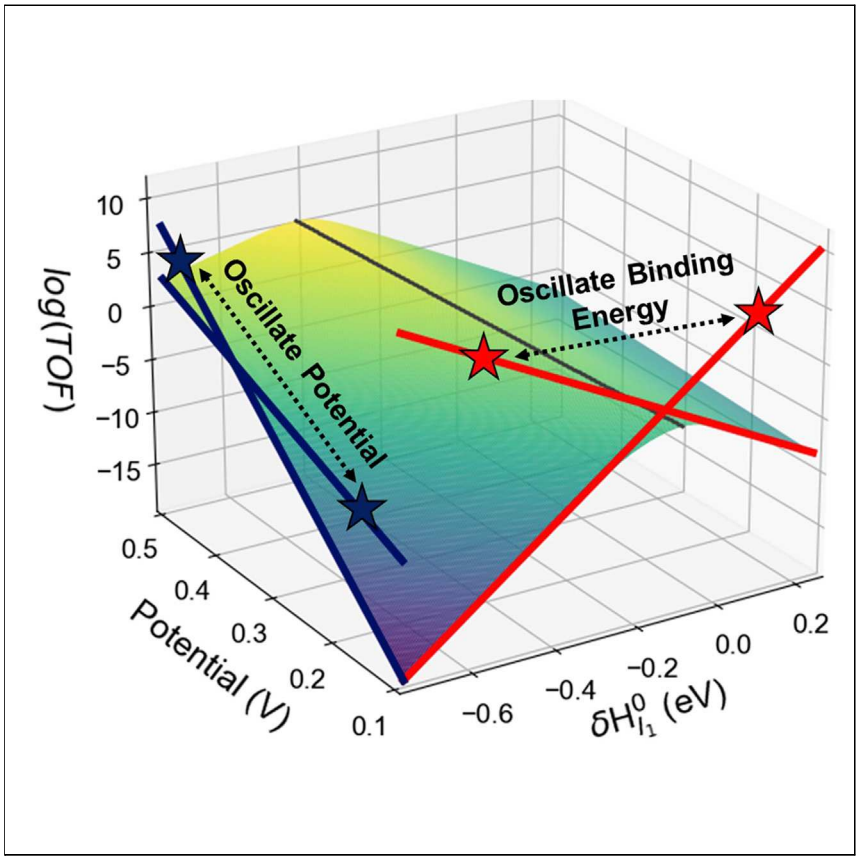

Certain electrocatalytic reactions can be accelerated by varying the applied potential with time. Requirements for this promotional effect are identified and contrasted with other approaches attempting to create catalysts that accelerate reaction rates with dynamically tunable surface properties.

Adam Baz, Mason Lyons, Adam Holewinski

adam.holewinski@colorado.edu

Highlights

Electrocatalytic reactions are evaluated under conditions of oscillating potential

Pure series reactions cannot exceed the steady-state rate at the highest potential

Parallel reactions can allow dynamic enhancement, but energy efficiency is sacrificed

Baz et al., Chem Catalysis 2, 3497–3516
December 15, 2022
https://doi.org/10.1016/j.checat.2022.09.002

Chem Catalysis

CellPress

Article

Dynamic electrocatalysis: Examining resonant catalytic rate enhancement under oscillating electrochemical potential

Adam Baz,[1,2] Mason Lyons,[1] and Adam Holewinski[1,2,3,*]

SUMMARY

A microkinetic analysis is presented for a generalized electrocatalytic reaction mechanism to evaluate whether oscillating electrochemical potential can be used to achieve resonant catalytic rate enhancement. It is illustrated that because changing the potential changes the free energy of reaction, this approach is conceptually distinct from oscillating binding energies of catalytic intermediates as within catalytic resonance theory. For faradaic reactions in series, no enhancements relative to the maximum steady-state turnover rate (within the potential range spanned by oscillation) are achievable, even in cases where the potential limits favor adsorption and desorption, respectively. It is possible to exceed a time-averaged steady-state rate (weighted by time at each condition), although only if the elementary reactions show disparate responses to potential. In contrast, if a faradaically driven parallel reaction controls surface coverage of a strongly adsorbed blocking species, significant dynamic enhancements over the maximum steady-state can be achieved, albeit at a cost of thermodynamic efficiency.

INTRODUCTION

Rational catalyst design has historically been informed by the heuristic known as the Sabatier principle, which states that an optimal catalyst should possess a moderate binding affinity toward the relevant adsorbed intermediates along a desired reaction pathway. A weakly binding material is limited by the rate of adsorption of reactants, while a strongly binding material is limited by the rate of desorption of products. Balancing between these necessary functionalities produces volcano-type behavior, where a moderate binding energy yields a maximum in the turnover frequency (TOF). Recently, several analyses have shown that this static Sabatier maximum can be overcome by dynamically varying the properties of the catalyst or operating conditions.[1] Through microkinetic simulations, Ardagh et al. showed that by oscillating between two binding energy states, distinct elementary steps can be driven at rates greater than those achievable under static conditions.[2] More specifically, for the mechanism in that work, a strong-binding condition facilitates adsorption and surface reaction, resulting in the accumulation of intermediates on the surface. Before the surface coverage becomes too high and time is "wasted" at this condition, the catalyst is transiently shifted to a weak-binding condition, facilitating the desorption of the accumulated intermediates to form products in the gas phase. Oscillating between these two states, with a waveform having amplitudes and frequencies in line with the intrinsic kinetics of the respective elementary steps, can then lead to the time-averaged TOF exceeding the TOF at an optimized static binding energy by several orders of magnitude. Further studies have shown that

THE BIGGER PICTURE

Recent simulations have shown that heterogeneous catalysts with dynamic properties—for example, the ability to vary adsorbate binding energy with time—could, in principle, give higher rates than an optimized catalyst operating at steady state (i.e., the Sabatier principle or "volcano curve" maximum, assuming typical correlations shaping the energy landscape of the reaction). Enhancements may be realized by oscillating catalyst properties at frequencies near the timescales of the elementary steps. Variation of electrochemical potential has been proposed as a possible method to induce such rate enhancements in electrocatalytic systems, but the extent to which this method could be effective has not been fully explored. Deeper understanding of electrochemical systems is also broadly critical, as electrocatalysis is well suited to utilize energy from renewables such as wind and solar power for the production of fuels, chemicals, and materials with low carbon intensity.

equilibrium conversion[3] and selectivity[4] can also be tuned by the dynamic oscillation of binding energy. Other work has investigated the implications of negative scaling relations on the possible rate enhancements achievable through oscillation of binding energy.[5] These cases were studied for a generalized $A \leftrightarrow A^* \leftrightarrow B^* \leftrightarrow B$ mechanism, and it was found that under a strong-binding A^* condition, desorption of B^* is facilitated, while under the weak-binding A^* condition, surface reaction from A^* to B^* is facilitated, which is qualitatively different behavior from the previously studied cases of positive scaling relations between the two surface intermediates.

A remaining challenge for dynamic catalysis is experimental implementation. However, a number of experimental methods have been proposed as possible stimuli to drive the oscillation of a catalyst between two binding energy states.[1] One example is mechanical oscillation of surface strain, which could be driven by intercalating ions into a catalyst substrate or utilization of a piezoelectric substrate to impart strain into a catalyst overlayer. Another method is the (non-faradaic) stimulation of thermochemical reactions using an electric field to manipulate adsorbate species with different dipole moments.[6] Photocatalytic routes have also been proposed, with photoexcitation of a surface resulting in transient charge transfer to or from adsorbates and triggering dissociation or desorption reactions; recent experiments toward this goal showed that pulsed illumination of Pt nanoparticles produced enhancement (relative to static illumination) in the rate of methanol decomposition to H_2.[7]

Dynamic electrocatalysis has similarly been proposed as a method to stimulate activity. This involves oscillation of an electrochemical potential as a means to drive a faradaic reaction to higher TOFs than would otherwise be achieved under static operation.[1] Several experimental works have shown that rate enhancements under dynamic potential oscillation are indeed observed for reactions including formic acid[8–10] and methanol[11–13] electro-oxidation. Similarly, the rate of the hydrogen oxidation reaction in the presence of trace CO impurities at the anode of a proton-exchange membrane (PEM) fuel cell can also be enhanced by pulsing to high anodic potentials to remove poisoning CO from the surface.[14] However, it is not yet established to what degree these enhancements can be attributed to resonant catalytic dynamics in the conventional sense—i.e., biasing some elementary steps at one potential condition (favoring intermediate accumulation) and other elementary steps at a different potential condition (favoring intermediate desorption). Also, the thermodynamic implications of utilizing potential as a means to drive catalytic rate enhancement have not been fully described. It is additionally worth mentioning that pulsed electrolysis has been used to modulate the mass transport of reactants to a surface for several electrochemical reactions including the electrosynthesis of adiponitrile[15] and electroreduction of CO_2,[16–18] but in this work, we choose to focus on the fundamental microkinetic response to potential oscillation as opposed to larger-scale effects such as mass transport.

RESULTS AND DISCUSSION

Microkinetic model

The primary model considered is a general three-step, series electrochemical oxidation mechanism outlined in reactions 1–3:

$$\text{R1: } R + (*) \leftrightarrow I_1^* + e^-,$$

$$\text{R2: } I_1^* \leftrightarrow I_2^* + e^-,$$

[1]Department of Chemical and Biological Engineering, University of Colorado Boulder, Boulder, CO 80303, USA

[2]Renewable and Sustainable Energy Institute, University of Colorado Boulder, Boulder, CO 80303, USA

[3]Lead contact

*Correspondence: adam.holewinski@colorado.edu

https://doi.org/10.1016/j.checat.2022.09.002

$$\text{R3: } I_2^* \leftrightarrow P + e^- + (*),$$

where R and P are reactant and product, respectively, in the fluid phase, and I_1^* and I_2^* are adsorbed intermediates. All reactions are faradaic, producing an electron upon each turnover of the elementary step. For simulations where a blocking/poisoning species is included, the following parallel elementary step is also considered:

$$\text{R4: } R_X + (*) \leftrightarrow I_X^* + e^-,$$

where R_X is a strongly adsorbing reactant and I_X^* is the adsorbed species that it forms, effectively blocking sites for the adsorption of intermediates I_1^* and I_2^*. This would be analogous, for example, to a surface becoming passivated by adsorbed oxygen from water. Other motifs are possible—for example, an undesired pathway forming strongly bound CO, which would be driven off (rather than onto) the surface at large potential. Such cases will have certain qualitative differences with the present analysis (such as whether the coverage rises or falls at a given condition), but the phenomena are not so disparate as to impact the main conclusions.

Rate constants of elementary steps are written according to transition state theory (TST):

$$k_i = \frac{k_B T}{h} \exp\left(\frac{\Delta S_i^{0,\ddagger}}{k_B}\right) \exp\left(\frac{-\Delta H_i^{0,\ddagger}}{k_B T}\right), \quad \text{(Equation 1)}$$

where $\Delta S_i^{0,\ddagger}$ and $\Delta H_i^{0,\ddagger}$ are the standard entropy and enthalpy of activation, respectively, of elementary step i at a given temperature and potential, and the other terms have their usual meanings. To capture the effect of changing binding energy (e.g., by changing material properties), we introduce γ_{j,j_D} as a generalized thermodynamic scaling parameter,[19,20] which represents how much the standard enthalpy of species j (enumerating reactant and product species) changes given a change in the standard enthalpy of an arbitrary descriptor intermediate, j_D, per the following relation:

$$H_j^{0,M,E_{ref}} = H_j^{0,M_{ref},E_{ref}} + \gamma_{j,j_D}\left(H_{j_D}^{0,M,E_{ref}} - H_{j_D}^{0,M_{ref},E_{ref}}\right) = H_j^{0,M_{ref},E_{ref}} + \gamma_{j,j_D}\delta H_{j_D}^0. \quad \text{(Equation 2)}$$

Here, $H_j^{0,M,E_{ref}}$ and $H_j^{0,M_{ref},E_{ref}}$ represent the standard enthalpy of intermediate j on a material M and a reference material M_{ref}, respectively, at a chosen reference potential. In our convention, H_j^0 for all intermediates and transition states are standard-state enthalpies relative to the stoichiometrically combined reactants as a zero-energy reference, such that the term $\delta H_{j_D}^0$ is analogous to the "$\Delta\Delta H$" term used in other works.[5] We reserve the uppercase Δ signifier to designate differences in enthalpy/entropy between initial states and transition or final states of elementary steps. We incorporate a Bronsted-Evans-Polanyi (BEP) transition state scaling parameter,[21,22] $\sigma_i \left(= \frac{\partial \Delta H_i^{0,\ddagger}}{\partial \Delta H_i^0}\right)$, and an electrochemical symmetry factor,[23,24] $\beta_i \left(= \frac{\partial \Delta H_i^{0,\ddagger}}{\partial E}\right)$, which describe the sensitivity of the activation barrier of the i^{th} elementary step to changes in its reaction energy and the electrochemical overpotential, respectively. In this formulation, the BEP term is restricted to contain pure chemical contributions to the reaction energy at a reference potential, while the potential dependence is explicitly separated to show its effect, as we have discussed previously.[25] The scaling factors σ_i and β_i are assumed constant in all cases here but do not have to be.[26] In more sophisticated kinetic models, potential and binding energy can cause variation of the symmetry and BEP coefficient values;[26] however, the magnitudes of the changes over typical oscillation amplitudes explored here should not be large enough to have major impacts on the conclusions of this work.[27] Incorporation of the material- and potential-dependent terms into the rate constant of each

elementary step yields the following expression, valid for each elementary step in a sequential, series faradaic reaction:

$$k_i = \frac{k_B T}{h}\exp\left(\frac{\Delta S_i^{0,\ddagger,M_{ref},E_{ref}}}{k_B}\right)\exp\left(\frac{-\left(\Delta H_i^{0,\ddagger,M_{ref},E_{ref}} - \beta_i n_i(E - E_{ref}) + \sigma_i\left(\gamma_{j_{final},j_D} - \gamma_{j_{initial},j_D}\right)\delta H_{j_D}^0\right)}{k_B T}\right), \quad \text{(Equation 3)}$$

where $\Delta S_i^{0,\ddagger,M_{ref},E_{ref}}$ and $\Delta H_i^{0,\ddagger,M_{ref},E_{ref}}$ are the standard entropy and enthalpy of activation, respectively, of elementary step i on a reference material, M_{ref}, at a reference potential, E_{ref}. n_i is the number of electrons transferred in elementary step i (always 1 here), and γ_{j_{final},j_D} and $\gamma_{j_{initial},j_D}$ are the thermodynamic scaling parameters of intermediate j in the final and initial states, respectively, of elementary step i. Equilibrium constants for each elementary step are similarly written as

$$K_i = \exp\left(\frac{\Delta S_i^{0,M_{ref},E_{ref}}}{k_B}\right)\exp\left(\frac{-\left(\Delta H_i^{0,M_{ref},E_{ref}} - n_i(E - E_{ref}) + \left(\gamma_{j_{final},j_D} - \gamma_{j_{initial},j_D}\right)\delta H_{j_D}^0\right)}{k_B T}\right), \quad \text{(Equation 4)}$$

where $\Delta S_i^{0,M_{ref},E_{ref}}$ and $\Delta H_i^{0,M_{ref},E_{ref}}$ are the standard entropy and enthalpy of reaction, respectively, on a reference material at a reference potential. Reverse rate constants are written as:

$$k_{-i} = \frac{k_i}{K_i}. \quad \text{(Equation 5)}$$

In the tested mechanism, I_1^* is set as the descriptor intermediate, such that $\delta H_{I_1}^0$ is the salient parameter describing all intermediate and transition state energies when deviating from the reference material (for a given set of thermodynamic and BEP scaling parameters). It is assumed that the standard entropies of activation/reaction are potential- and material independent and that the effects of potential are limited to faradaic contributions (i.e., electric field or other secondary effects on the adsorption enthalpies[28,29] of intermediates are ignored). Adsorbate-adsorbate interactions are also not incorporated into the model.

The mean-field approximation is applied, leading to the following ordinary differential equations (ODEs) modeling the propagation of the species coverages in time:

$$\frac{d\theta_{I_1}}{dt} = k_{1f} a_R \theta_* - k_{1r}\theta_{I_1} - k_{2f}\theta_{I_1} + k_{2r}\theta_{I_2}, \quad \text{(Equation 6)}$$

$$\frac{d\theta_{I_2}}{dt} = k_{2f}\theta_{I_1} - k_{2r}\theta_{I_2} - k_{3f}\theta_{I_2} + k_{3r} a_P \theta_*. \quad \text{(Equation 7)}$$

And for cases where poisoning species are included,

$$\frac{d\theta_{I_X}}{dt} = k_{Xf} a_{R_X}\theta_* - k_{Xr}\theta_{I_X}. \quad \text{(Equation 8)}$$

Using the solved (steady state or transient) coverages, the net forward rate of each elementary reaction is defined as

$$r_1 = k_{1f} a_R \theta_* - k_{1r}\theta_{I_1}, \quad \text{(Equation 9)}$$

$$r_2 = k_{2f}\theta_{I_1} - k_{2r}\theta_{I_2}, \quad \text{(Equation 10)}$$

$$r_3 = k_{3f}\theta_{I_2} - k_{3r} a_P \theta_*. \quad \text{(Equation 11)}$$

The rate of production of P and e^- can then be written as

$$r_P = r_3, \quad \text{(Equation 12)}$$

$$r_{e^-} = r_1 + r_2 + r_3. \quad \text{(Equation 13)}$$

Campbell's generalized degree of rate control (DRC) is used throughout the work to analyze the extent to which different species (transition states or surface intermediates) control the rate of reaction. The DRC[30,31] is defined as

$$X_i = \left.\frac{\partial \ln(r)}{\partial\left(-G_i^0/RT\right)}\right|_{G^o_{j\neq i}}, \quad \text{(Equation 14)}$$

where G_i^0 is the standard-state Gibbs free energy of species i, which is perturbed while holding $G^0_{j\neq i}$ constant. The DRC measures the change in the rate of reaction induced by a differential decrease in the standard-state Gibbs free energy (divided by R times T) of a given species in the mechanism. It has been proven that all transition state DRCs sum to unity.[32] Therefore, a transition state with a DRC = 1 can be interpreted as fully rate determining. For intermediate species, the DRC is typically negative or 0, and it is related to the fractional surface coverage of the species. For a mechanism wherein all elementary steps each involve one catalytic site (*), the DRC of each intermediate species has been proven to be equal to the negative of the coverage of that species,[32,33] which allows us to refer to these quantities interchangeably throughout the work. It has also been shown that the DRCs can be used to predict various macrokinetic observables of thermo- and electro-catalytic reactions.[34–36]

The temporal dynamics of a square-wave oscillation (of either binding energy, $\delta H^0_{l_1}$, or potential, E) are defined by the frequency (f) in s^{-1} and the duty cycle (DC), given by

$$f = \frac{1}{t_1 + t_2}, \quad \text{(Equation 15)}$$

$$DC = \frac{t_2}{t_1 + t_2} \times 100. \quad \text{(Equation 16)}$$

All dynamic systems are integrated in time until the dynamic steady state (DSS) is reached. The average TOF of a system under DSS is calculated as

$$TOF_{DSS} = \frac{\int_0^{t_1+t_2} TOF(t)dt}{t_1 + t_2}, \quad \text{(Equation 17)}$$

where the initial time point of the first cycle under DSS is treated as time zero and $TOF(t)$ is the instantaneous TOF during dynamic operation. DSS can be simplified in the limit of $f \to 0$, which yields the time-weighted average of the steady-state TOF at the two oscillation conditions:

$$TOF_{DSS,f\to 0} = \frac{\int_0^{t_1+t_2} TOF_{f\to 0}(t)dt}{t_1 + t_2} = \frac{(t_1 \times TOF_{SS,1}) + (t_2 \times TOF_{SS,2})}{t_1 + t_2}. \quad \text{(Equation 18)}$$

Two kinds of enhancement factors for the TOF may then be defined. The first is the enhancement, under DSS, relative to the time-weighted average steady state (DSS as $f \to 0$):

$$EF_{SS_{AVG}} = \frac{TOF_{DSS}}{TOF_{DSS,f\to 0}} = \frac{TOF_{DSS}}{TOF_{SS_{AVG}}}. \quad \text{(Equation 19)}$$

This metric provides a measure of the gains imparted by approaching catalytic resonance in the strictest sense, such that only "extra" turnovers from the transient relaxation periods are counted. The second enhancement factor is the enhancement relative to the maximum steady-state TOF over the oscillation window ($TOF_{SS_{MAX}}$):

$$EF_{SS_{MAX}} = \frac{TOF_{DSS}}{TOF_{SS_{MAX}}}. \quad \text{(Equation 20)}$$

This metric analyzes the extent to which an oscillation of potential or binding energy yields activity greater than the static Sabatier maximum. We note here that for simple series mechanisms, this maximum will occur at the largest magnitude of overpotential in the operation window. For these cases, rate may be driven arbitrarily higher by increasing the overpotential further (at the expense of thermodynamic efficiency), and so it is not particularly informative. On the other hand, we will encounter for parallel mechanisms that there can be a maximum steady-state rate at intermediate overpotential, making $EF_{SS_{MAX}}$ a useful characterization tool.

An electrochemical energy efficiency, *EE*, may also be defined if we construct a hypothetical full electrolytic cell, where the half-cell oxidation reaction outlined in reactions (R1–R4) occurs at the anode and an arbitrary, kinetically facile reduction reaction occurs at the cathode. For convenience, we designate the cathode as the hydrogen evolution reaction (HER) with a standard half-cell potential of $E^0_{\text{cathode}} = 0.0\ V_{SHE}$. We then assign an (arbitrary) standard half-cell potential for the anodic reaction to be $E^0_{anode} = 1.0\ V_{SHE}$, which sets the full cell open-circuit potential to $E_{OCP} = 1.0\ V$, which is on the right order for many electrolytic reactions of contemporary interest. When analyzing the single anodic half-cell reaction in the following kinetic analysis, the choice of reference electrode is arbitrary, so for simplicity we designate $E_{ref} = 1.0\ V_{SHE}$ such that the anodic reaction is in equilibrium at 0 *V vs.* E_{ref}. The electrochemical energy efficiency can then be written as

$$EE = \frac{\int (TOF_e(t) \times E_{OCP})dt}{\int (TOF_e(t) \times E(t))dt} \times 100, \quad \text{(Equation 21)}$$

where $TOF_e(t)$ is the instantaneous TOF toward the production of electrons (from r_{e^-} above) and $E(t)$ is the instantaneous cell potential. We finally define a dynamic efficiency gain metric to describe any loss or improvement in electrochemical energy efficiency during DSS relative to the average steady state

$$\Delta EE(\%) = EE_{DSS} - EE_{SS_{AVG}}, \quad \text{(Equation 22)}$$

where ΔEE may take on negative values in the situations where operation under DSS results in a loss of efficiency relative to the *EE* for SS_{AVG}. Without reference to a specific reaction, these efficiencies are only meant to be interpreted qualitatively in terms of gain or loss; a larger E_{OCP} decreases the percentage loss corresponding to a given overpotential, and vice versa.

Pure series mechanism

The pure series mechanism considered is outlined in reactions (R1–R3) in the section microkinetic model. The general forms of the rate and equilibrium constants, as well as the definitions for parameters describing the rates, enhancement factors, and efficiencies under dynamic conditions, are outlined in detail in the section microkinetic model as well. Species activities are set here to $a_R = 1$ and $a_P = 0.001$ in order to simulate far-from-equilibrium reaction conditions under differential conversion (i.e., negligible product re-adsorption and reverse reaction). The temperature (in all simulations unless otherwise stated) is set to $T = 298.15\ K$. The reference energies (with

Table 1. Standard-state enthalpies and entropies (at the reference potential and on the reference material) of each of the species considered in the mechanism in reactions (R1–R4)

Species	$R(f)$	TS_1	l_1^*	TS_2	$l_{l_2}^*$	TS_3	$P(f)$	$R_X(f)$	TS_X	l_x*
$H^{0,M_{ref},E_{ref}}$ (eV)	0	0.70	−0.30	0.55	−0.30	0.70	0	0	0.50	−0.20
$S^{0,M_{ref},E_{ref}}\left(\frac{meV}{K}\right)$	0	−0.5	−1.0	−1.0	−1.0	−0.5	0	0	−0.5	−1.0

These values are held constant for all simulations unless otherwise noted.

respect to material/binding energy and potential) are outlined in Table 1 and are maintained for all simulations unless otherwise stated. The reference energies in Table 1 were chosen so that under a reference base case with zero overpotential and the descriptor adsorption energy equal to zero, all steps would have similar degrees of rate control. Below, we first establish the effects of oscillating binding energy in order to draw parallels to prior simulations of dynamic thermocatalytic systems. These results are then contrasted with oscillation of electrochemical potential.

Oscillation of binding energy

To understand the sensitivity of the system toward various kinetic parameters, it is helpful to first consider the steady-state behavior as a function of binding energy (specifically, $\delta H_{l_1}^0$) and potential, E, shown in Figure 1. Here, the kinetic parameters have been chosen to give similar sensitivity of the two steps to both potential and binding energy. This is a common estimate based on the constraint that all symmetry factors and BEP scaling coefficients should vary between 0 and 1; values here are each fixed to 0.5 ($\beta_1 = \beta_2 = \beta_3 = \sigma_1 = \sigma_2 = \sigma_3 = 0.5$). The thermodynamic scaling parameter $\gamma_{l_2^*,l_1^*}$ is also set to 0.5; this parameter may be fractional or exceed 1 (and in some cases may be negative[5]) depending on the choice of descriptor species. On all figure panels, the two white "x" markers correspond to two binding energy conditions, namely $\delta H_{l_1}^0 = -0.25$ and +0.25 eV, which are oscillated between in a square waveform during dynamic catalysis simulations at a constant potential of $E = 0.1$ V versus E_{ref} (all potentials will be referenced with respect to E_{ref} from here on).

Figure 1A shows the TOF activity map with respect to the production of P as a function of $\delta H_{l_1}^0$ and E. The volcano curves (moving left to right) are nearly symmetric with respect to binding energy and maintain this symmetry across all potentials. In other words, the effect of increasing potential is not to appreciably change the location of the peak of the volcano (with respect to $\delta H_{l_1}^0$) but instead to increase the TOF at all $\delta H_{l_1}^0$ values. The reason for this symmetry can be seen by analyzing the DRCs for each of the species in the mechanism, which are shown in Figures 1B–1F. For all exothermic binding energies, the surface transitions from being populated by l_1^*, at low potentials, to l_1^* and l_2^* sharing equal surface coverages of ~0.5 at larger overpotentials. On the weak-binding side of the volcano, the surface is uniformly dominated by free sites. Between the two binding energy oscillation point markers, the rate-controlling transition state changes from TS_3 (at strong-binding conditions) to TS_1 (at weak-binding conditions). When TS_3 is primarily rate controlling, the surface coverage of l_1^* is high, and when TS_1 is rate controlling, the surface is empty, indicating a relationship between the DRCs of transition states and the stable surface intermediates. We observe that a change in steady-state surface coverage can only be induced by a change in the relative DRCs of the transition state species in the mechanism. Since resonant catalytic rate enhancement requires the accumulation of intermediates at one condition (strong binding) and subsequent desorption to product at another condition (weak binding), consequently, the DRCs of the respective

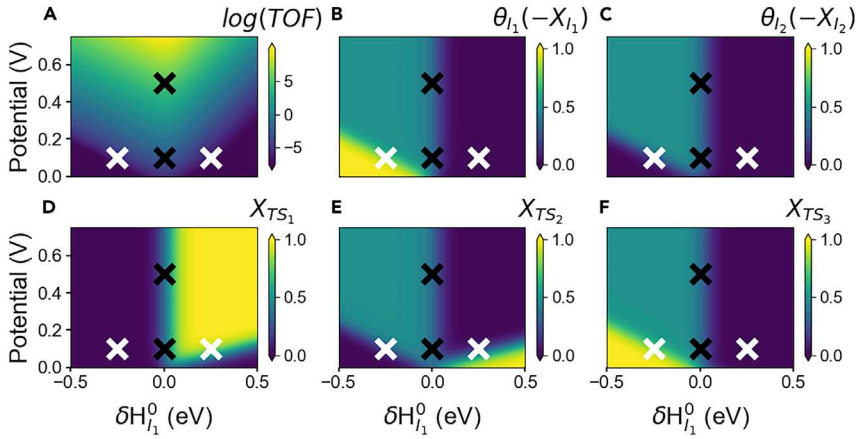

Figure 1. Steady-state activity maps, coverages, and degrees of rate control for "symmetric" electrochemical symmetry factors

In all subplots, $\beta_1 = \beta_2 = \beta_3 = \sigma_1 = \sigma_2 = \sigma_3 = \gamma_{I_2^*,I_1^*} = 0.5$. Black "x" markers correspond to an oscillation condition for potential ($E = 0.1\ V \leftrightarrow E = 0.5\ V$) at constant binding energy ($\delta H^0_{I_1} = 0\ eV$), and white "x" markers correspond to an oscillation of binding energy ($\delta H^0_{I_1} = -0.25\ eV \leftrightarrow \delta H^0_{I_1} = +0.25\ eV$) at constant potential ($E = 0.1\ V$).

(A) TOF activity map (with respect to the production of P; TOF toward the production of e^- is greater by a constant factor of 3× at all conditions).

(B) Coverage of I_1^*, equal to the negative of the DRC of I_1^*.

(C) Coverage of I_2^*, equal to the negative of the DRC of I_2^*.

(D) DRC of TS_1.

(E) DRC of TS_2.

(F) DRC of TS_3.

transition state species must be changed as a function of the oscillation condition (binding energy or potential) to produce resonant enhancement. Since the transition state DRCs are different at each of the two white "x" markers, one would expect an oscillation of binding energy between these two points to possibly bring about a rate enhancement relative to the static Sabatier maximum between the two points. The same cannot be said for the two black "x" markers, which are representative of a potential oscillation at constant binding energy.

Figure 2 shows the results of a dynamic catalysis simulation, oscillating between the two white "x" marker points on Figure 1 at a frequency of $f = 0.1$ Hz and a duty cycle of $DC = 50\%$, with all other kinetic parameters from Figure 1 held the same. Figure 2A shows the free energy diagrams at the two conditions, with the strong-binding limit ($\delta H^0_{I_1} = -0.25$ eV) in blue and weak-binding limit ($\delta H^0_{I_1} = +0.25$ eV) in black. The binding energy square waveform is indicated as a function of the number of cycles in Figure 2B. Figure 2C shows the coverages of all surface intermediates, with the dynamic and steady-state coverages indicated by solid and dashed lines, respectively. At the strong-binding condition, the coverage of I_1^* begins near unity and then decreases as it is converted to I_2^*. Before I_1^* and I_2^* can approach their steady-state values (~0.8 and ~0.2, respectively), the system is shifted to the weak-binding condition, which results in a monotonic decrease in the coverage of I_1^* and a subsequent increase, then decrease, in the coverage of I_2^*. Once the surface is completely cleared, the adsorption of I_1^* begins again with the next cycle, as the catalyst is shifted to the strong-binding condition. Figure 2D shows the instantaneous (solid) and steady-state (dashed) TOFs with respect to the formation of product P and electrons e^-, which are distinguishable since electrons are formed from the turnover of each elementary step, while product P is only formed with the turnover of elementary

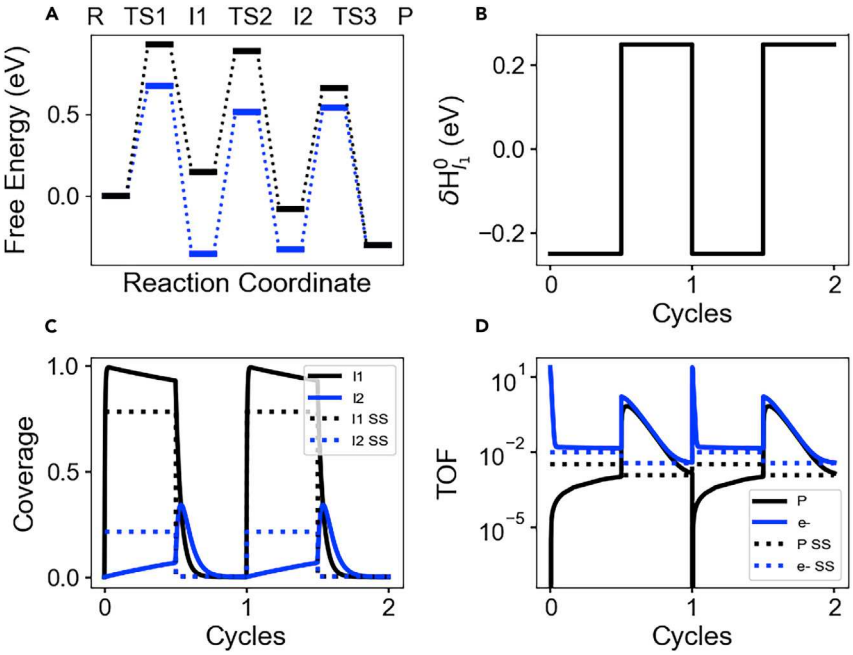

Figure 2. Dynamic catalysis simulation under oscillating binding energy

Kinetic parameters are $\beta_1 = \beta_2 = \beta_3 = \sigma_1 = \sigma_2 = \sigma_3 = \gamma_{I_2^*,I_1^*} = 0.5$. Duty cycle 50%, frequency 0.1 Hz.

(A) Free-energy diagrams corresponding to two binding energy conditions in a dynamic catalysis simulation ($\delta H_{I_1}^0 = -0.25$ eV, blue, $\delta H_{I_1}^0 = +0.25$ eV, black) at a constant potential of $E = 0.1$ V.

(B) Binding energy waveform during dynamic catalysis.

(C) Coverages of all surface intermediates during binding energy oscillations.

(D) Dynamic and steady-state TOFs with respect to the production of P and e^-.

step 3. The TOF with respect to product P increases and decays after shifting to the weak-binding condition since the accumulated intermediates are desorbed to product at this condition. The TOF with respect to e^- also increases and decays upon the shift to weak binding, with an additional spike occurring after the next transition back to strong binding. The cause of this behavior is elucidated in Figure S1, which shows the individual rates of each elementary step with respect to the TOF for forming e^-. After each shift from strong to weak binding, the rates of elementary steps 2 and 3 increase, due to the promotion of conversion of I_1^* to I_2^* and subsequent desorption of I_2^*. The net forward rate of elementary step 1 becomes negative, since at this condition, the high coverage of I_1^* and the endergonic nature of the elementary step result in its backward rate being greater than its forward rate. After the shift from weak to strong binding, the rate of elementary step 1 spikes, corresponding to the fast adsorption of I_1^* and concomitant production of e^-. The steady-state TOFs with respect to products P and e^-, shown against the dynamic TOFs in Figure 2D, are significantly lower than the dynamic TOFs during the weak-binding condition, indicating that the off-loading of accumulated product during dynamic catalysis is creating the enhancements in the TOFs over the steady-state condition.

We may then extend the analysis to a wider range of binding energy frequencies and amplitudes while still holding constant the set of kinetic parameters used to construct Figures 1 and 2. The enhancement factors, relative to the average steady state ($EF_{SS_{AVG}}$) and the maximum steady state ($EF_{SS_{MAX}}$) over each binding energy range, are displayed in Figures 3A and 3B, respectively. At amplitudes near $\delta H_{I_1}^0 = \pm 0.4$ eV and

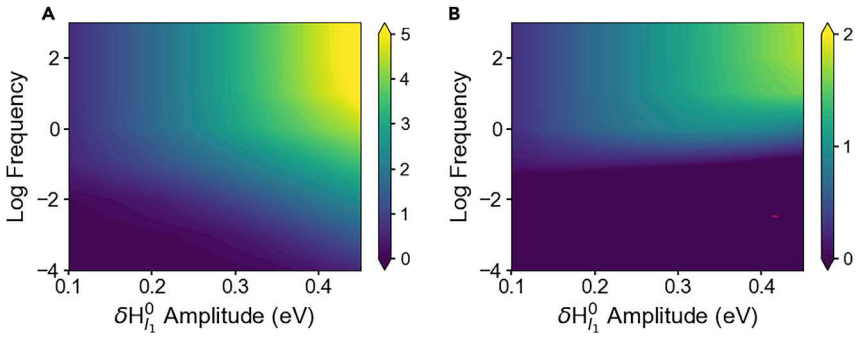

Figure 3. Dynamic catalysis enhancement heat maps under oscillating binding energy

Simulated over ranges of $\delta H_{I_1}^0$ amplitudes (centered around a $\delta H_{I_1}^0$ = 0 eV) and frequencies (duty cycle = 50%) at a constant potential of E = 0.1 V. Kinetic parameters are $\beta_1 = \beta_2 = \beta_3 = \sigma_1 = \sigma_2 = \sigma_3 = \gamma_{I_2^*,I_1^*} = 0.5$.

(A and B) (A) $Log_{10}\ EF_{SS_{AVG}}$ and (B) $Log_{10}\ EF_{SS_{MAX}}$ with respect to the production of product P. A log enhancement factor of 0 (i.e., no enhancement) is set as the lower limit on both color bar scales so that regions of low $EF_{SS_{MAX}}$ do not interfere with highlighting the regions of enhancement.

frequencies in the range of 10–1,000 Hz, the average dynamic TOFs are roughly four to five orders of magnitude greater than the average of the TOFs at the two steady-state conditions. At the same amplitude/frequency ranges, these average dynamic TOFs are roughly 1 to 2 orders of magnitude greater than the maximum/optimal steady-state TOF over the binding energy range. These results corroborate those found by Ardagh et al., wherein oscillations of binding energy allow one to achieve significant enhancements over the optimal, static Sabatier maximum rate at several frequency and amplitude combinations.[2]

Oscillation of potential

Next, we consider the oscillation of potential between the two black "x" markers outlined on each of the heat maps in Figure 1. This entails traversing along the peak of the Sabatier volcano from a low potential, 0.1 V, to a higher potential, 0.5 V, at a constant binding energy of $\delta H_{I_1}^0$ = 0 eV. The free-energy diagrams corresponding to these two potential conditions are shown in Figure 4A. The major difference from the oscillating binding energy case is that the overall reaction free energy is driven downhill as potential is increased. All three elementary step barriers are also driven downhill equally, since in this case, the symmetry factors are identical for each step. This differs from the behavior of the oscillating binding energy system, where a strengthening/weakening of binding energy accelerates some elementary steps at the expense of others. The oscillating-potential results are consistent with the steady-state DRCs from Figure 1, which indicate that the transition state and intermediate DRCs are identical at 0.1 and 0.5 V (at a constant binding energy of $\delta H_{I_1}^0$ = 0 eV). This manifests in identical coverages of intermediates I_1^* and I_2^* at the two steady-state conditions. Accordingly, the coverages do not change during dynamic operation either, as shown in Figure 4C. The result is that the dynamic TOFs, in all cases, are identical to the steady-state TOFs at both conditions. While the rate is significantly increased at high potential, there are no additional benefits from transiently switching between the two potential conditions. This also results in the electrochemical energy efficiency metric (*EE*) being identical for the steady-state and transient operations. This behavior is maintained for a wide range of potential amplitudes and frequencies, as shown in Figure S2.

It may be noted that there are some regions on the activity maps from Figure 1 where a change in potential at constant binding energy does result in a change in some of

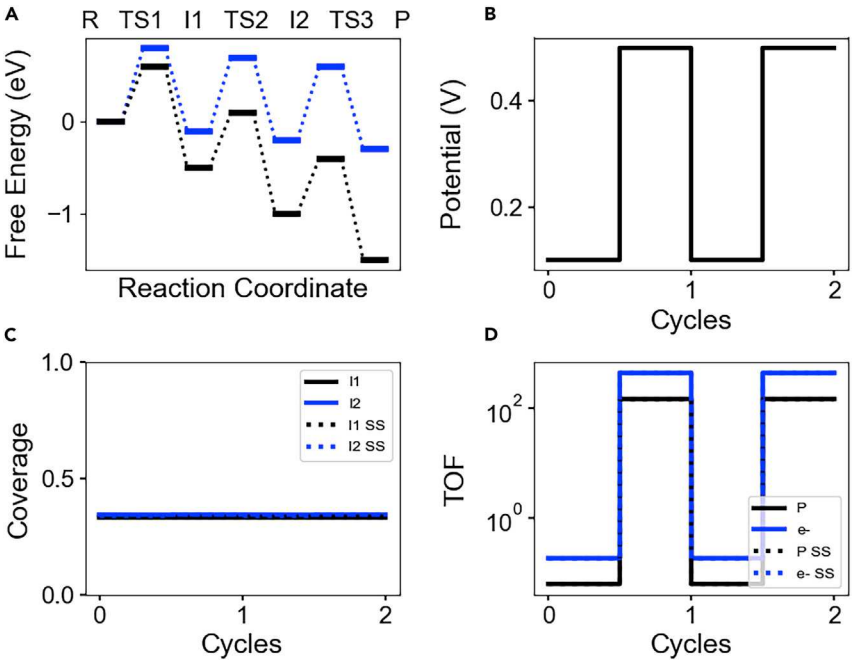

Figure 4. Dynamic catalysis simulation under oscillating potential with identical symmetry factors

Kinetic parameters are $\beta_1 = \beta_2 = \beta_3 = \sigma_1 = \sigma_2 = \sigma_3 = \gamma_{I_2^*,I_1^*} = 0.5$. Duty cycle 50%, frequency 1 Hz.

(A) Free-energy diagram corresponding to two potentials in a dynamic catalysis simulation (E = 0.1 V, blue, E = 0.5 V, black) with "symmetric" barriers at a constant descriptor binding energy of $\delta H_{I_1}^0 = 0$ eV.

(B) Transient potential during dynamic catalysis.

(C) Coverages of all surface intermediates during potential oscillations.

(D) Dynamic and steady-state TOFs with respect to the production of P and e^-.

the transition state and intermediate DRCs. At exothermic binding energies—for instance, $\delta H_{I_1}^0 = -0.3$ eV—moving from 0.1 to 0.5 V results in a change from TS_3 being almost entirely rate controlling at 0.1 V to TS_2 and TS_3 sharing equal degrees of rate control at 0.5 V, resulting in a change in the coverage of intermediates (nearly covered by I_1^* at low potential, and equal populations of I_1^* and I_2^* at higher potential; see Figure S3). However, a simulation of dynamic catalysis between these two conditions still does not produce any enhancements with respect to either the average or maximum steady state, and the electrochemical efficiency is unaffected (see Figures S4 and S5). At low potential, I_2^* is simply converted back into I_1^*, while at high potential, I_1^* converts to I_2^* until the two species approach nearly equal coverages. Here, the excursion to low potential provides no benefit in terms of facilitating the adsorption/accumulation of intermediates; it simply changes the distribution of coverages between the two intermediates via $I_2^* \leftrightarrow I_1^*$, but the total coverage remains constant.

Looking back to the case of oscillating binding energy, it is clear from the plots of coverage in Figures 1B and 1C that the strong-binding condition favors the accumulation of adsorbates, while the weak-binding condition favors their desorption. One might then similarly expect that for an oscillation of potential to induce a rate or efficiency enhancement, one potential condition must prefer the adsorption of intermediates and the other must prefer desorption. This could be expected for situations where the potential sensitivities (i.e., the symmetry factors) for each of the elementary step barriers are different. For example, a case where the adsorption

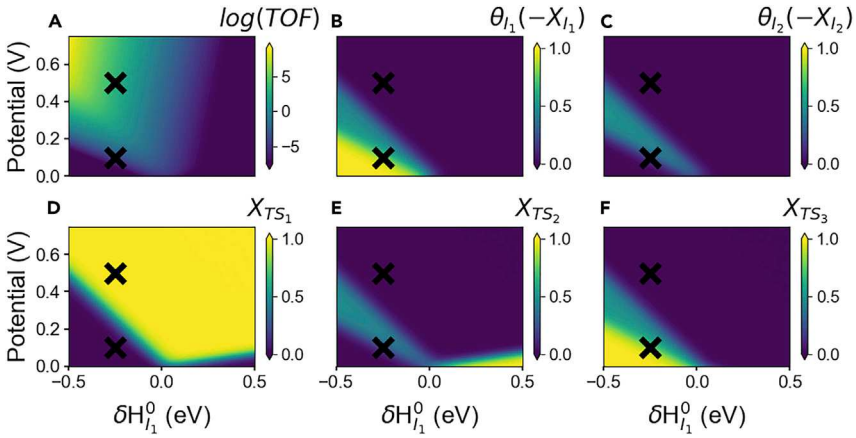

Figure 5. Steady-state activity maps, coverages, and degrees of rate control for "asymmetric" electrochemical symmetry factors

In all subplots, $\beta_1 = 0.1$, $\beta_2 = 0.9$, $\beta_3 = 0.9$, $\sigma_1 = \sigma_2 = \sigma_3 = \gamma_{I_2^*,I_1^*} = 0.5$. Black "x" markers correspond to a potential oscillation condition ($E = 0.1$ V ↔ $E = 0.5$ V) at constant binding energy ($\delta H^0_{I_1} = -0.25$ eV).

(A) TOF activity map (with respect to the production of *P*; TOF toward the production of e^- is greater by a constant factor of 3 at all conditions).

(B) Coverage of I_1^*, equal to the negative of the DRC of I_1^*.

(C) Coverage of I_2^*, equal to the negative of the DRC of I_2^*.

(D) DRC of TS_1.

(E) DRC of TS_2.

(F) DRC of TS_3.

step responds weakly to potential ($\beta_1 \rightarrow 0$), while the surface reaction and desorption steps respond strongly to potential ($\beta_2, \beta_3 \rightarrow 1$), should favor adsorption at low potential and surface reaction/desorption at high potential. Under these conditions, one may accumulate intermediates at low potential to reach a coverage greater than would be produced under the high-potential condition (at steady state) and then shift to the high-potential condition to react and desorb the accumulated intermediates at a higher rate, due to the decreased barriers for surface reaction and desorption. A steady-state analysis of the series reaction mechanism (reactions R1–R3) with an "asymmetric" set of symmetry factors ($\beta_1 = 0.1$, $\beta_2 = 0.9$, $\beta_3 = 0.9$, $\sigma_1 = \sigma_2 = \sigma_3 = \gamma_{I_2^*,I_1^*} = 0.5$) is shown in Figure 5, with the two black "x" markers indicating the points of oscillation in potential. The BEP and thermodynamic scaling parameters are kept constant here to isolate the effect of varying the electrochemical symmetry factors. The activity map is no longer symmetric with respect to binding energy, although the rate does still increase monotonically with potential at all binding energies. Across the range of the potential oscillation (centered at a constant binding energy of $\delta H^0_{I_1} = -0.25$ eV), the primary rate controlling species shifts from TS_3 at low potential, to TS_2 at intermediate potential, and finally to TS_1 at high potential. This results in the accumulation of I_1^* at low potential, followed by its conversion to I_2^* at intermediate potential, and finally to an empty surface at the high-potential limit. Based on this steady-state behavior, we expect an oscillation between the two potential points to induce a rate enhancement relative to the average steady-state condition.

Figure 6 displays the results of a dynamic catalysis simulation corresponding to the kinetic parameter set used to construct Figure 5. The free-energy diagram illustrates the implications of the variable symmetry factors—the barrier for the adsorption step

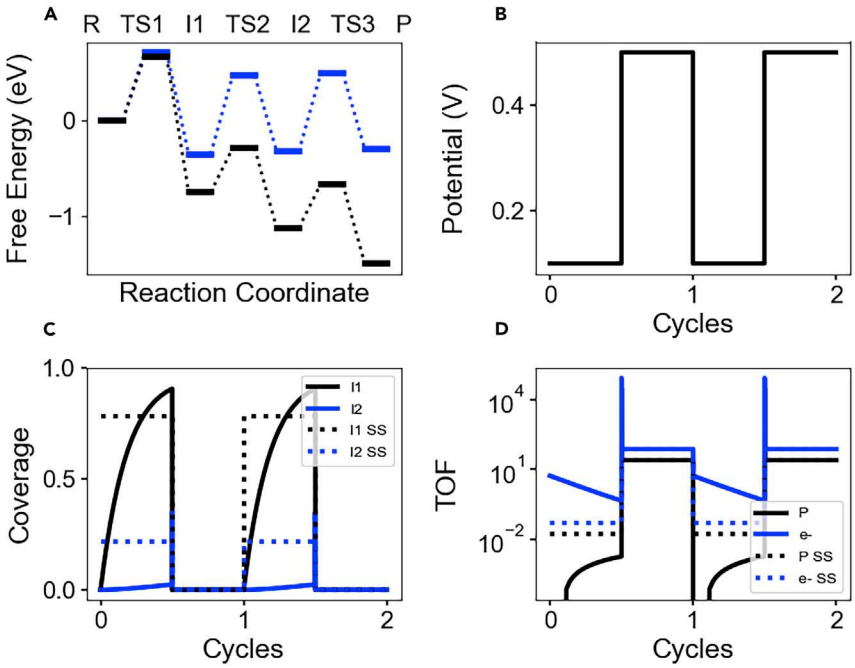

Figure 6. Dynamic catalysis simulation under oscillating potential with disparate symmetry factors

Kinetic parameters are $\beta_1 = 0.1$, $\beta_2 = 0.9$, $\beta_3 = 0.9$, $\sigma_1 = \sigma_2 = \sigma_3 = \gamma_{I_2^*,I_1^*} = 0.5$. Duty cycle 50%, frequency 1 Hz.

(A) Free-energy diagram corresponding to two potentials in a dynamic catalysis simulation with "asymmetric" electrochemical symmetry factors ($E = 0.1$ V, blue, $E = 0.5$ V, black) at a constant descriptor binding energy of $\delta H_{I_1}^0 = -0.25$ eV.

(B) Transient potential during dynamic catalysis.

(C) Coverages of all surface intermediates during potential oscillations.

(D) Dynamic and steady-state TOFs with respect to the production of P and e^-.

is nearly constant at both potentials, while the barriers for the surface reaction and desorption steps are significantly reduced at higher potential. It should be emphasized, however, that this scenario is still conceptually distinct from the oscillation of binding energy, since all steps are driven downhill when potential is increased (as opposed to some becoming more endergonic, and some more exergonic, for variation in binding energy). Low potential favors the accumulation of I_1^*, while at high potential, both I_1^* and I_2^* are quickly (relative to the frequency of oscillation, 1 Hz) desorbed to form product. This results in a spike in the TOF with respect to both P and e^- when the potential is switched to 0.5 V, as shown in Figure 6D. The main contributions to this spike are from elementary reactions 2 and 3—namely, surface reaction and desorption, both of which produce e^- as indicated in Figure S6. Notably, the spike in TOF induced by shifting to higher potential is higher than the steady-state TOF at the high-potential condition.

To assess the impact of waveform and prospects for catalytic resonance, the kinetic parameter set of Figures 5 and 6 is next studied over a range of potential amplitudes and frequencies in Figure 7A (constant binding energy of $\delta H_{I_1}^0 = -0.25$ eV; duty cycle 50%). A small enhancement (about 33% increase) relative to the average steady-state TOF toward the production of P can be seen around potential amplitudes of ± 0.1 V and frequencies around 100 Hz. While this enhancement is small relative to those observed when oscillating binding energy, the underlying limitation comes

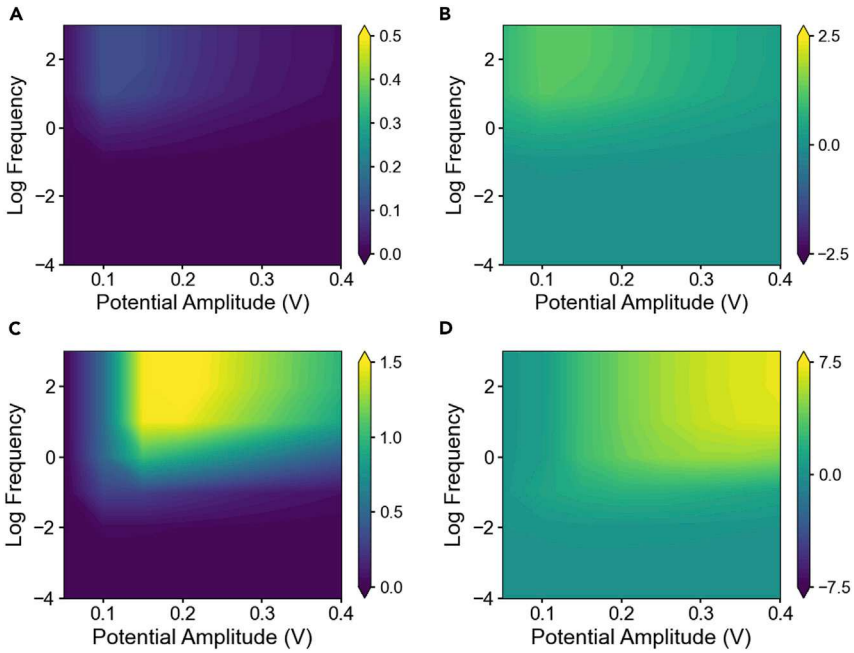

Figure 7. Dynamic catalysis enhancement heatmaps under oscillating potential

Simulated over ranges of ΔE amplitudes and frequencies with a constant binding energy of $\delta H^0_{I_1} = -0.25$ eV. Kinetic parameters are $\beta_1 = 0.1$, $\beta_2 = 0.9$, $\beta_3 = 0.9$, $\sigma_1 = \sigma_2 = \sigma_3 = \gamma_{I_2^*,I_1^*} = 0.5$.

(A) $\mathrm{Log}_{10}\, EF_{SS_{AVG}}$ with respect to production of P, duty cycle = 50%.

(B) Corresponding energy efficiency gain (ΔEE), duty cycle = 50%.

(C) $\mathrm{Log}_{10}\, EF_{SS_{AVG}}$ with respect to production of P, duty cycle = 0.5%.

(D) Corresponding ΔEE, duty cycle = 0.5%.

largely from the fact that the duty cycle is set to 50%. Returning to the particular example of a 1 Hz oscillation from 0.1 to 0.5 V shown in Figure 6, "spikes" in the production of P (seen when the accumulated intermediates desorb at high potential) occur over such a small time span that the average TOF toward production of P per cycle is barely affected. However, it can be seen in the coverage plots (Figure 6C) that nearly the entire time span at the lower potential limit is required to accumulate an appreciable number of intermediates. This time imbalance between the loading of intermediates at low potential (slow process) and their unloading at high potential (fast process) is expected to persist for other combinations of potential amplitude and frequency because the condition of larger overpotential raises the rate constant for all steps. Ideally, one would spend a larger fraction of the time in a given cycle at the low potential, since the process occurring (here, adsorption) will always be slower than the process that is favored at higher potential (here, surface reaction/desorption). Then, the system would only spend a small fraction of time at high potential to unload the accumulated intermediates before returning to the low-potential condition. Interestingly, the number of "extra" electron turnovers (above steady-state production) that occur at the low-potential condition slightly outnumber those at the high-potential condition for this balanced duty cycle scenario. This results in a small relative energy efficiency gain of about 1% (Figure 7B).

Adjusting the duty cycle to 0.5% (i.e., 0.5% of the waveform spent at the high-potential condition) leads to improvements in the TOF enhancement factor relative to the average steady state. Figures 7C and 7D shows these metrics for the case of a 0.5% duty cycle (same kinetic parameters as used for the 50% duty cycle analysis in

Figures 7A and 7B). In this case, the average TOF can be enhanced by about a factor of 37× at potential amplitudes of 0.2 V and frequencies of 100–1,000 Hz. The rate improvements are due to a better balancing of the time spent operating at the two potential conditions. The energy efficiency remains negligibly impacted near the optimal amplitude, though at larger amplitudes, a modest efficiency gain is notable, again due to more "extra" turnovers occurring at the low-potential condition, while the surface immediately is cleared by the very large upper potential limits. The variation of amplitude is discussed further in Figures S8–S10, which show induction periods for establishment of DSS coverages and mark the corresponding potential limits on replicas of Figures 5 and 7C. The results of a further reduction in duty cycle to 0.01% (time spent at high potential) are shown in Figure S7. Enhancements relative to the average steady state reach about 250×, and the frequencies and amplitudes that result in this gain correspond with losses of efficiency (ΔEE) around 15%. The efficiency trade-off is due to the appropriately balanced (for rate) duty cycle leading to a larger fraction of the "extra" electrons now being passed at the high-potential condition.

An important distinction remains to be made between the cases of oscillating potential versus oscillating binding energy. In all cases studied thus far, under no conditions can an oscillation in potential create TOFs that are greater than the static Sabatier maximum over a given potential range. Enhancements in TOF or efficiency are only achieved relative to the time-weighted average steady-state behavior at the two potential conditions. This is due to the fact that the TOF always increases monotonically (and rapidly so) with potential for a series, faradaic reaction where all steps are electrochemical in nature. However, this does raise a question as to the source of experimentally observed rate enhancements (relative to the "optimal" steady state over a given potential range) observed for some electrochemical reactions. Most notably, these include the electro-oxidation of small organics such as methanol and formic acid. These reactions differ from the simple series mechanism, however, in that they each contain parallel pathways and may also contain site-blocking spectator species. For instance, OH* or O* surface species are typically formed at high potentials (e.g. > 0.8 V versus RHE on platinum catalysts) during each of these reactions.[25] These adsorbed O species block sites for formic acid activation, and even though they participate in the case of methanol oxidation, their overaccumulation at high potential also deactivates the catalyst. In the next section, we extend the model to include the possibility of the adsorption of a faradaically driven spectator species.[37] We acknowledge that this generalized model is simplified relative to the aforementioned organic electro-oxidations, but it captures the most critical phenomena and provides insight into how site-blocking spectator species influence the prospects for resonant enhancement in electrocatalytic systems.

Mechanism including spectator species

Here, we consider the same mechanism from the section microkinetic model, except we now include the adsorption of I^*_X per reaction (R4), which is a spectator ad species that blocks sites for the preferred pathway (reactions (R1–R3)). Once again, we start with a steady-state analysis, which is presented in Figure 8, for the "symmetric" electrochemical symmetry factor case. The major qualitative difference from the pure series mechanism is that the TOF no longer monotonically increases as a function of potential. This is due to the accumulation of I^*_X as potential is increased, indicated on the coverage plot in Figure 8D. This produces a volcano-shaped activity map (in both dimensions now; Figure 8A) with a peak at intermediate potentials and binding energies. We also see that the DRC of TS_1 increases with potential, which was not observed in the absence of the spectator ad species. As the surface becomes

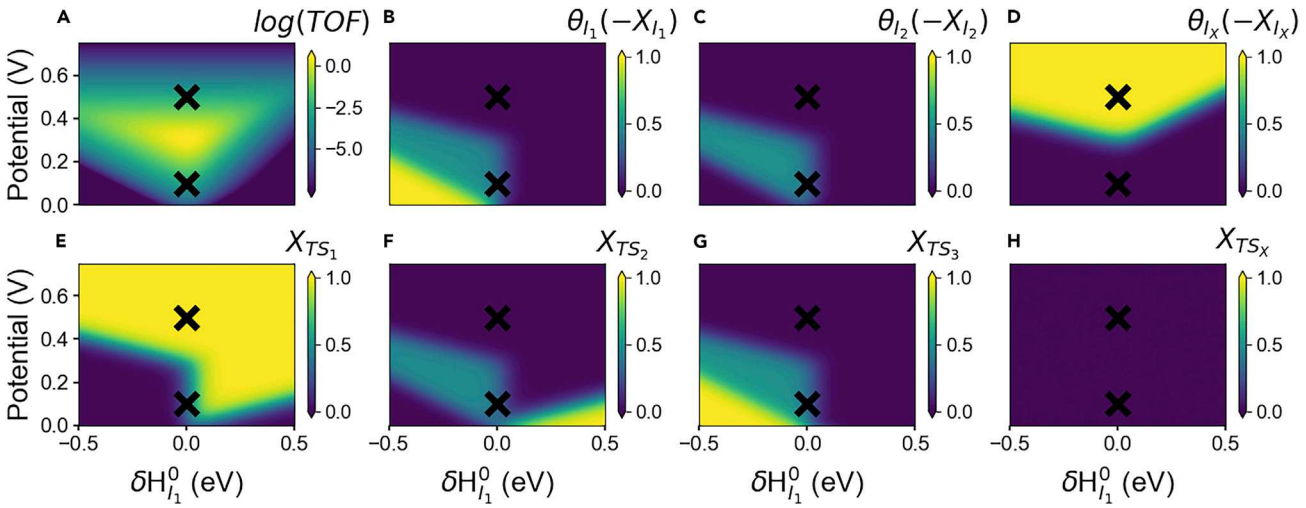

Figure 8. Steady-state activity maps, coverages, and degrees of rate control for mechanism containing site-blocking spectator species

In all subplots, $\beta_1 = \beta_2 = \beta_3 = \beta_X = \sigma_1 = \sigma_2 = \sigma_3 = \sigma_X = \gamma_{I_2^*,I_1^*} = \gamma_{I_X^*,I_1^*} = 0.5$ and $a_{R_X} = 1 \times 10^{-3}$. Black "x" markers correspond to a potential oscillation condition ($E = 0.1$ V ↔ $E = 0.5$ V) at a constant binding energy of $\delta H^0_{I_1} = 0$ eV.

(A) TOF activity map (with respect to the production of *P*).

(B) Coverage of I_1^*, equal to the negative of the DRC of I_1^*.

(C) Coverage of I_2^*, equal to the negative of the DRC of I_2^*.

(D) Coverage of I_X^*, equal to the negative of the DRC of I_X^*.

(E) DRC of TS_1.

(F) DRC of TS_2.

(G) DRC of TS_3.

(H) DRC of TS_X.

increasingly saturated with I_X^*, the adsorption of I_1^* becomes commensurately rate limiting since it must compete for sites as a prerequisite for subsequent turnover to *P*. The highest Sabatier maximum is found at intermediate potential because this balances two competing effects—the increased potential speeds up the rate of the preferred pathway, but at too high of a potential, I_X^* accumulates and decreases the activity. Therefore, one may expect that by oscillating between two potential points on either side of the static maximum, the system would achieve a high rate on the preferred path for a certain amount of time, until I_X^* accumulates and begins to decrease the rate. By returning to low potential, I_X^* desorbs, freeing up sites for the next cycle.

A dynamic catalysis simulation, oscillating potential between the two black "x" marker conditions on Figure 8 (and for the same kinetic parameter set), is shown in Figure 9. All conditions are identical to those studied in Figures 1 and 4, except the frequency is set to 10 Hz and the spectator-adsorption elementary step is included. When the potential is stepped to 0.5 V, the coverages of I_1^* and I_2^* briefly spike but then decrease, due to being outcompeted by I_X^* for sites. This produces spikes in the TOFs (with respect to *P* and e^-) that are significantly larger than the steady-state TOFs during the high-potential condition, as shown in Figure 9D. Analyzing this same system over a range of frequencies and potential amplitudes (Figure 10), one can see that at amplitudes of $\Delta E = \pm 0.4$ V and frequencies >100 Hz, the average dynamic TOFs are nearly three orders of magnitude greater than their average steady-state counterparts. The average dynamic TOFs are also greater (by roughly 50×) than the static Sabatier maximum TOF over the oscillation-potential range. This type of enhancement was not observed for any oscillating-potential system in the case of pure series reactions. However, the

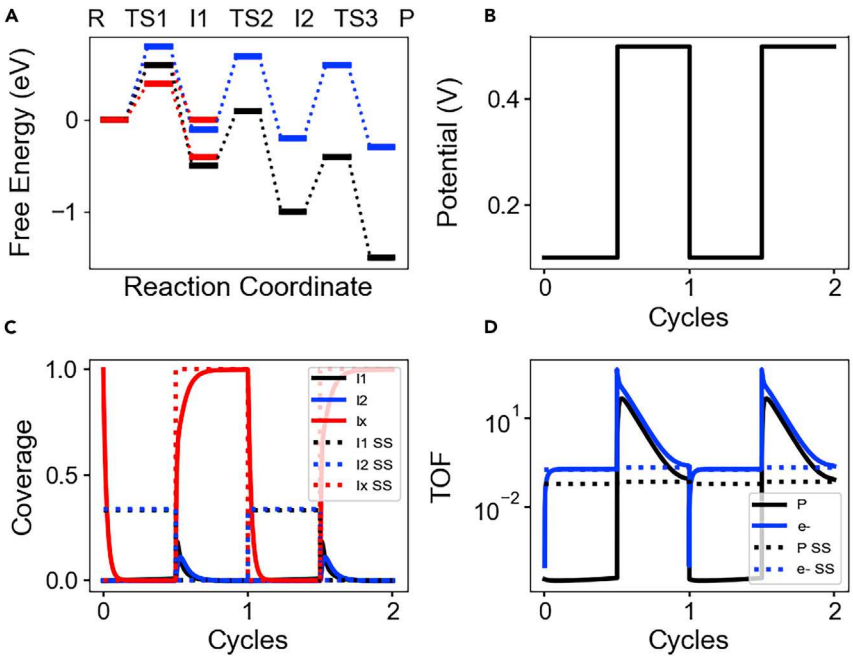

Figure 9. Dynamic catalysis simulation under oscillating potential for mechanism containing site-blocking spectator species

Kinetic parameters are $\beta_1 = \beta_2 = \beta_3 = \beta_X = \sigma_1 = \sigma_2 = \sigma_3 = \sigma_X = \gamma_{I_2^t,I_1^t} = \gamma_{I_X^t,I_1^t} = 0.5$. Duty cycle 50%, frequency 10 Hz.

(A) Free-energy diagram corresponding to the two potential conditions for dynamic catalysis (E = 0.1 V, blue, E = 0.5 V, black) at a constant binding energy of $\delta H_{I_1}^0 = 0$ eV. Red lines overlayed on the diagram correspond to the spectator species at both potential conditions.

(B) Transient potential during dynamic catalysis.

(C) Coverages of all surface intermediates during potential oscillations.

(D) Dynamic and steady-state TOFs with respect to the production of P and e^-.

electrochemical energy efficiencies shown in Figure 10C indicate that the rate enhancements at the high-potential condition lead to a significant reduction in the efficiency when operating under dynamic conditions—more current is again passed at a large overpotential relative to the thermodynamic equilibrium potential. Therefore, TOFs greater than those corresponding to the static Sabatier maximum may be achieved, but they come at the cost of thermodynamic efficiency.

Conclusions

Herein, we have illustrated the effects of oscillating electrochemical potential in the context of achieving catalytic rate enhancements. For a faradaic, series mechanism, enhancements relative to the average steady-state TOFs at the two potential limits of a square waveform were found to be possible, provided that the elementary steps associated with raising and lowering intermediate coverages have different elementary symmetry factors. Small enhancements in thermodynamic efficiency are also possible, but no enhancements occur relative to the maximum steady-state TOF across the potential range. Conversely, when a faradaically driven spectator ad species is incorporated into the mechanism, enhancements can be achieved relative to both the average and maximum steady-state TOFs. However, these enhancements come at the cost of a loss in thermodynamic efficiency, since a larger fraction of electrons are produced at the higher potential condition, relative to the average steady-state operation.

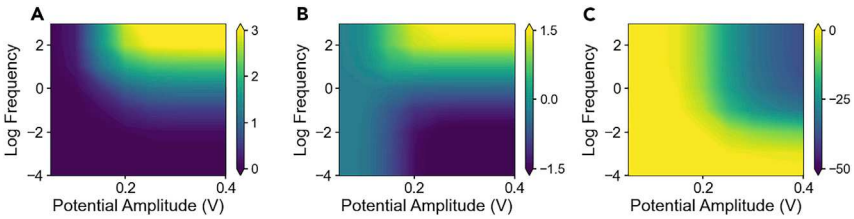

Figure 10. Dynamic catalysis enhancement heatmaps under oscillating potential for mechanism containing site-blocking spectator species

Simulated over ranges of ΔE amplitudes and frequencies (duty cycle = 50%) with a constant binding energy of $\delta H_{I_1}^0 = 0$ eV. Kinetic parameters are $\beta_1 = \beta_2 = \beta_3 = \beta_X = \sigma_1 = \sigma_2 = \sigma_3 = \sigma_X = \gamma_{I_2^*,I_1^*} = \gamma_{I_X^*,I_1^*} = 0.5$.

(A) $\mathrm{Log}_{10}\, EF_{SS_{AVG}}$ with respect to production of product *P*.

(B) $\mathrm{Log}_{10}\, EF_{SS_{MAX}}$ with respect to the production of product *P*.

(C) Gain in electrochemical energy efficiency, ΔEE (linear scale).

Based on these observations, we suggest that if the product of an electrochemical reaction has high enough value to outweigh costs of lost efficiency, there could be advantages to dynamic operation in permitting the use of smaller, lower-cost reactors. This said, there may be penalties paid beyond the pure kinetic losses, for example, in the form of extra ohmic losses. Additionally, if the timescales of elementary steps approach those of the time constant for electrochemical double layer charging or begin to have an interplay with mass transport of reactants, then the associated phenomena and resulting complexities must also be considered. For example, typical double layer time constants on the order of ms to μs would complicate operation at oscillation frequencies approaching 10^3 to 10^6 Hz, respectively. Frequencies at or above the double-layer timescale are not likely characteristic of any experimentally enhanced systems observed to date—the cases of organic oxidation reactions studied thus far have typically observed enhancements in the range of 1–1,000 Hz[8,12] with double-layer time constants closer to the μs range. Oscillation near the timescale of double-layer charging would mainly manifest in phase shifts between the potential and current, with higher frequencies leading to pure capacitive current.

EXPERIMENTAL PROCEDURES

Resource availability

Lead contact

Further information and requests for resources should be directed to and will be fulfilled by the lead contact, Adam Holewinski (adam.holewinski@colorado.edu).

Materials availability

This study did not generate new unique reagents.

Data and code availability

The code generated during this study is available at the following GitHub repository (https://github.com/adambaz/Baz-Holewinski-Dynamic-Electrocatalysis) and is publicly available at the date of this publication.

Computational details

For all dynamic (transient) kinetic systems described in the results and discussion, the system of ODEs was integrated using the *DifferentialEquations.jl* library[38] in the Julia coding language using the "RadauIIA5" solver with relative and absolute tolerances of 1×10^{-8}. Square-wave oscillations of binding energy and potential are modeled

by solving the system of ODEs at each binding energy/potential condition for periods of time dictated by the frequency and duty cycle of the oscillation. The adsorbate coverages from the final time point of the system integration at the first binding energy/potential are used as the initial conditions for the integration at the second set of conditions. This is repeated for many cycles until the system reaches DSS, where the integrated rates at the end of two subsequent cycles are identical within a certain percentage tolerance (1×10^{-11}%). An example of the coverages during this "induction period" is shown in Figure S8. For steady-state systems, the time derivatives in Equations 6, 7 and 8 are set equal to 0, yielding a system of non-linear algebraic equations that are solved using the *NLsolve.jl* library[39] applying a Newton root-finding algorithm with a tolerance of 1×10^{-60}.

SUPPLEMENTAL INFORMATION

Supplemental information can be found online at https://doi.org/10.1016/j.checat.2022.09.002.

ACKNOWLEDGMENTS

The authors acknowledge support from the National Science Foundation (CBET 1944834).

AUTHOR CONTRIBUTIONS

Conceptualization, A.B. and A.H.; methodology, A.B. and A.H.; investigation, A.B. and M.L.; writing – original draft, A.B.; writing – review & editing, A.B., M.L., and A.H.; supervision, A.H.

DECLARATION OF INTERESTS

The authors declare no competing financial interest.

Received: June 22, 2022
Revised: August 8, 2022
Accepted: August 31, 2022
Published: September 21, 2022

REFERENCES

1. Shetty, M., Walton, A., Gathmann, S.R., Ardagh, M.A., Gopeesingh, J., Resasco, J., Birol, T., Zhang, Q., Tsapatsis, M., Vlachos, D.G., et al. (2020). The catalytic mechanics of dynamic surfaces: stimulating methods for promoting catalytic resonance. ACS Catal. *10*, 12666–12695. https://doi.org/10.1021/acscatal.0c03336.

2. Ardagh, M.A., Abdelrahman, O.A., and Dauenhauer, P.J. (2019). Principles of dynamic heterogeneous catalysis: surface resonance and turnover frequency response. ACS Catal. *9*, 6929–6937.

3. Ardagh, M.A., Birol, T., Zhang, Q., Abdelrahman, O.A., and Dauenhauer, P.J. (2019). Catalytic resonance theory: SuperVolcanoes, catalytic molecular pumps, and oscillatory steady state. Catal. Sci. Technol. *9*, 5058–5076. https://doi.org/10.1039/c9cy01543d.

4. Ardagh, M.A., Shetty, M., Kuznetsov, A., Zhang, Q., Christopher, P., Vlachos, D.G., Abdelrahman, O.A., and Dauenhauer, P.J. (2020). Catalytic resonance theory: parallel reaction pathway control. Chem. Sci. *11*, 3501–3510. https://doi.org/10.1039/c9sc06140a.

5. Gathmann, S.R., Ardagh, M.A., and Dauenhauer, P.J. (2022). Catalytic resonance theory: negative dynamic surfaces for programmable catalysts. Chem. Catal. *2*, 140–163. https://doi.org/10.1016/j.checat.2021.12.006.

6. Shetty, M., Ardagh, M.A., Pang, Y., Abdelrahman, O.A., and Dauenhauer, P.J. (2020). Electric-field-assisted modulation of surface thermochemistry. ACS Catal. *10*, 12867–12880. https://doi.org/10.1021/acscatal.0c02124.

7. Qi, J., Resasco, J., Robatjazi, H., Alvarez, I.B., Abdelrahman, O., Dauenhauer, P., and Christopher, P. (2020). Dynamic control of elementary step energetics via pulsed illumination enhances photocatalysis on metal nanoparticles. ACS Energy Lett. *5*, 3518–3525. https://doi.org/10.1021/acsenergylett.0c01978.

8. Gopeesingh, J., Ardagh, M.A., Shetty, M., Burke, S.T., Dauenhauer, P.J., and Abdelrahman, O.A. (2020). Resonance-promoted formic acid oxidation via dynamic electrocatalytic modulation. ACS Catal. *10*, 9932–9942. https://doi.org/10.1021/acscatal.0c02201.

9. Román, A.M., Spivey, T.D., Medlin, J.W., and Holewinski, A. (2020). Accelerating electro-oxidation turnover rates via potential-modulated stimulation of electrocatalytic activity. Ind. Eng. Chem. Res. *59*, 19999–20010. https://doi.org/10.1021/acs.iecr.0c04414.

10. Adžić, R.R., Popov, K.I., and Pamić, M.A. (1978). Acceleration of electrocatalytic reactions by pulsation of potential: oxidation of formic acid on Pt and Pt/pbads electrodes. Electrochim. Acta *23*, 1191–1196.

11. Fedkiw, P.S., Traynelis, C.L., and Wang, S. (1988). Pulsed-potential oxidation of methanol. J. Electrochem. Soc. *135*, 2459–2465.

12. Wang, S., and Fedkiw, P.S. (1992). Pulsed-potential oxidation of methanol I. Smooth

platinum electrode with and without tin surface modification. J. Electrochem. Soc. *139*, 2519–2525.

13. Wang, S., and Fedkiw, P.S. (1992). Pulsed-potential oxidation of methanol II. Graphite-supported platinum electrode with and without tin surface modification. J. Electrochem. Soc. *139*, 3151–3158.

14. Carrette, L.P.L., Friedrich, K.A., Huber, M., and Stimming, U. (2001). Improvement of CO tolerance of proton exchange membrane (PEM) fuel cells by a pulsing technique. Phys. Chem. Chem. Phys. *3*, 320–324. https://doi.org/10.1039/b005843m.

15. Blanco, D.E., Lee, B., and Modestino, M.A. (2019). Optimizing organic electrosynthesis through controlled voltage dosing and artificial intelligence. Proc. Natl. Acad. Sci. USA *116*, 17683–17689. https://doi.org/10.1073/pnas.1909985116.

16. Kim, C., Weng, L.C., and Bell, A.T. (2020). Impact of pulsed electrochemical reduction of CO2on the formation of C2+Products over Cu. ACS Catal. *10*, 12403–12413. https://doi.org/10.1021/acscatal.0c02915.

17. Bui, J.C., Kim, C., Weber, A.Z., and Bell, A.T. (2021). Dynamic boundary layer simulation of pulsed CO2Electrolysis on a copper catalyst. ACS Energy Lett. *6*, 1181–1188. https://doi.org/10.1021/acsenergylett.1c00364.

18. Engelbrecht, A., Uhlig, C., Stark, O., Hämmerle, M., Schmid, G., Magori, E., Wiesner-Fleischer, K., Fleischer, M., and Moos, R. (2018). On the electrochemical CO 2 reduction at copper sheet electrodes with enhanced long-term stability by pulsed electrolysis. J. Electrochem. Soc. *165*, J3059–J3068. https://doi.org/10.1149/2.0091815jes.

19. Montemore, M.M., and Medlin, J.W. (2014). Scaling relations between adsorption energies for computational screening and design of catalysts. Catal. Sci. Technol. *4*, 3748–3761. https://doi.org/10.1039/C4CY00335G.

20. Greeley, J. (2016). Theoretical heterogeneous catalysis: scaling relationships and computational catalyst design. Annu. Rev. Chem. Biomol. Eng. *7*, 605–635. https://doi.org/10.1146/annurev-chembioeng-080615-034413.

21. Wang, S., Petzold, V., Tripkovic, V., Kleis, J., Howalt, J.G., Skúlason, E., Fernández, E.M., Hvolbæk, B., Jones, G., Toftelund, A., et al. (2011). Universal transition state scaling relations for (de)hydrogenation over transition metals. Phys. Chem. Chem. Phys. *13*, 20760–20765. https://doi.org/10.1039/c1cp20547a.

22. Nørskov, J.K., Bligaard, T., Hvolbæk, B., Abild-Pedersen, F., Chorkendorff, I., and Christensen, C.H. (2008). The nature of the active site in heterogeneous metal catalysis. Chem. Soc. Rev. *37*, 2163–2171. https://doi.org/10.1039/b800260f.

23. Bard, A.J., and Faulkner, L.R. (2001). Electrochemical Methods: Fundamentals and Applications Second (John Wiley & Sons, Inc.).

24. Guidelli, R., Compton, R.G., Feliu, J.M., Gileadi, E., Lipkowski, J., Schmickler, W., and Trasatti, S. (2014). Defining the transfer coefficient in electrochemistry: an assessment (IUPAC Technical Report). Pure Appl. Chem. *86*, 245–258. https://doi.org/10.1515/pac-2014-5026.

25. Baz, A., and Holewinski, A. (2020). Understanding the interplay of bifunctional and electronic effects: microkinetic modeling of the CO electro-oxidation reaction. J. Catal. *384*, 1–13. https://doi.org/10.1016/j.jcat.2020.02.003.

26. Zhang, J., Tao, H.B., Kuang, M., Yang, H.B., Cai, W., Yan, Q., Mao, Q., and Liu, B. (2020). Advances in thermodynamic-kinetic model for analyzing the oxygen evolution reaction. ACS Catal. *10*, 8597–8610. https://doi.org/10.1021/acscatal.0c01906.

27. Román, A.M., Dudoff, J., Baz, A., and Holewinski, A. (2017). Identifying " optimal " electrocatalysts: impact of operating potential and charge transfer model. ACS Catal. *7*, 8641–8652. https://doi.org/10.1021/acscatal.7b03235.

28. Chen, L.D., Urushihara, M., Chan, K., and Nørskov, J.K. (2016). Electric field effects in electrochemical CO2 reduction. ACS Catal. *6*, 7133–7139. https://doi.org/10.1021/acscatal.6b02299.

29. Karlberg, G.S., Rossmeisl, J., and Nørskov, J.K. (2007). Estimations of electric field effects on the oxygen reduction reaction based on the density functional theory. Phys. Chem. Chem. Phys. *9*, 5158–5161. https://doi.org/10.1039/b705938h.

30. Campbell, C.T. (2017). The degree of rate control : a powerful tool for catalysis research. ACS Catal. *7*, 2770–2779. https://doi.org/10.1021/acscatal.7b00115.

31. Stegelmann, C., Andreasen, A., and Campbell, C.T. (2009). Degree of rate control: how much the energies of intermediates and transition states control rates. J. Am. Chem. Soc. *131*, 8077–8082. https://doi.org/10.1021/ja9000097.

32. Foley, B.L., and Bhan, A. (2020). Degree of rate control and De Donder relations – an interpretation based on transition state theory. J. Catal. *384*, 231–251. https://doi.org/10.1016/j.jcat.2020.02.008.

33. Mao, Z., and Campbell, C.T. (2020). The degree of rate control of catalyst-bound intermediates in catalytic reaction mechanisms: relationship to site coverage. J. Catal. *381*, 53–62. https://doi.org/10.1016/j.jcat.2019.09.044.

34. Mao, Z., and Campbell, C.T. (2019). Apparent activation energies in complex reaction mechanisms: a simple relationship via degrees of rate control. ACS Catal. *9*, 9465–9473. https://doi.org/10.1021/acscatal.9b02761.

35. Mao, Z., and Campbell, C.T. (2020). Kinetic isotope effects: interpretation and prediction using degrees of rate control. ACS Catal. *10*, 4181–4192. https://doi.org/10.1021/acscatal.9b05637.

36. Baz, A., and Holewinski, A. (2021). Predicting macro-kinetic observables with the generalized degree of rate control in electrocatalysis. J. Catal. *397*, 233–244. https://doi.org/10.1016/j.jcat.2021.03.014.

37. Román, A.M., Hasse, J.C., Medlin, J.W., and Holewinski, A. (2019). Elucidating acidic electro-oxidation pathways of furfural on platinum. ACS Catal. *9*, 10305–10316. https://doi.org/10.1021/acscatal.9b02656.

38. Rackauckas, C., and Nie, Q. (2017). DifferentialEquations.jl – a performant and feature-rich ecosystem for solving differential equations in Julia. J. Open Res. Softw. *5*, 15. https://doi.org/10.5334/jors.151.

39. Mogensen, P.K., and Riseth, A.N. (2018). Optim: a mathematical optimization package for Julia. J. Open Source Softw. *3*, 615. https://doi.org/10.21105/joss.00615.